PAPER • OPEN ACCESS

Fuel retention and carbon deposition on beryllium marker tiles from JET tokamak main chamber limiters investigated by ion beam analysis

OPEN ACCESS
IOP Publishing | International Atomic Energy Agency Nuclear Fusion

Nucl. Fusion **62** (2022) 126070 (9pp) https://doi.org/10.1088/1741-4326/ac9cf0

Fuel retention and carbon deposition on beryllium marker tiles from JET tokamak main chamber limiters investigated by ion beam analysis

P. Tsavalas[1,2], A. Lagoyannis[1], K. Mergia[1,*], M. Axiotis[1], S. Harissopulos[1], G. Provatas[3], S. Fazinić[3], T. Tadić[3], A. Widdowson[4], M. Rubel[5] and JET Contributors[a]

[1] National Centre for Scientific Research 'Demokritos', 15310 Aghia Paraskevi, Athens, Greece
[2] Department of Physics, Zografou Campus, National Technical University of Athens, Athens, Greece
[3] Ruđer Bošković Institute, Bijenička 54, 10000 Zagreb, Croatia
[4] United Kingdom Atomic Energy Authority, Culham Science Centre, Abingdon, OX14 3DB, United Kingdom
[5] KTH Royal Institute of Technology, Fusion Plasma Physics, 100 44 Stockholm, Sweden

E-mail: kmergia@ipta.demokritos.gr

Received 12 July 2022, revised 30 September 2022
Accepted for publication 24 October 2022
Published 15 November 2022

Abstract

The JET tokamak with the ITER-like wall is operated with arrays of castellated beryllium (Be) limiters in the main chamber. In several locations Be marker tiles were installed for erosion-deposition studies. The castellation sides and the plasma-facing surfaces (PFSs) of Be marker tiles from three different locations of the JET main chamber, from the experimental campaigns 2011–12 (ILW-1) and 2013–14 (ILW-2), were analysed, employing ^{2}H and ^{3}He micro-beams in order to determine carbon (C) impurity deposition and deuterium (D) retention. The deposited C and D amounts on the castellation sides (up to 1.5 mm deep into the groove) were assessed with respect to the ion/electron drift direction. Both the C and D amounts on the investigated castellation sides either stay constant or reduce with depth from the edge of the PFS. No systematic difference is observed in the C deposition or D retention on the different castellation sides of each sample with respect to the ion/electron drift direction. C and D content is found to be lower on the PFS than on surfaces in the gaps of castellation for the majority of the samples. The C amount is, in general, higher than the D one. No systematic correlation between the C and the D amounts has been observed.

Keywords: JET tokamak, beryllium, deuterium retention, ion beam analysis, carbon deposition

(Some figures may appear in colour only in the online journal)

* Author to whom any correspondence should be addressed.
[a] See Joffrin *et al* 2019 (https://doi.org/10.1088/1741-4326/ab2276) for the JET Contributors.

1. Introduction

The choice of appropriate plasma-facing materials (PFMs) is an issue of great importance as the plasma-wall interaction affects both the lifetime of wall materials and plasma performance. Beryllium (Be) and tungsten (W) are the materials for plasma facing components (PFCs) in ITER [1]. Be has been chosen due to its low atomic number which limits plasma dilution and energy radiation losses. This metal has high thermal conductivity ($\sim$200 Wm^{-1} K^{-1}), low fuel retention in comparison to carbon (C) which reacts chemically with H isotopes [2] and it is an efficient oxygen-getter, thus reducing oxygen impurities, and helps to keep the effective atomic number, Z_{eff}, in the vessel at low levels. A detailed overview of Be as PFC is presented in [3].

Until 2009 the Joint European Torus (JET) at the Culham Science Centre, the largest tokamak in the world, was operated with C as the main PFM (JET-C) [4]. Very high fuel inventories were measured because the presence of C is decisive for fuel retention by co-deposition [5]. This called for a large-scale test of a metal wall. Since 2011 JET has metallic PFC, called the ITER-like wall (JET-ILW) [6]. Be is in the main chamber (castellated limiters and Be coatings on the inner wall cladding) and W in the divertor: the load bearing plate in the base made of bulk metal, while W-coated C fiber composites (CFCs) tiles are in other locations. Three experimental campaigns were performed in 2011–2016 with deuterium (D) fuelling: 2011–12 (ILW-1), 2013–14 (ILW-2) and 2015–16 (ILW-3) with input energy of 150, 201 and 245 GJ, respectively. The overview has been presented in [7], while detailed works have dealt with erosion, material deposition and D retention on the surface of the divertor [8–18] and on the main chamber [19–26]. In addition, material deposition and fuel retention on surfaces located in the gaps of the castellated Be limiters have been examined [27–29]. It has also been consistently shown that fuel inventory with ILW was reduced by one order of magnitude in comparison to JET-C [30, 31]. The main source of C in JET was eliminated, but still the knowledge of the C content in co-deposits and the C–D correlation is crucial for the detailed assessment of factors influencing the retention in JET-ILW and, by this, for improved predictions for ITER. Two are the sources of C after the JET transformation to a fully metallic device, (a) the C residuals from the previous wall and (b) the CFC tiles coated by W in the divertor [32].

The relation between material deposition and D retention in JET-ILW had been investigated in detail on W-coated divertor tiles. Works [10, 12, 14, 24] report that the retention increases with the increase of the material (Be and C) deposition. The works [13, 15–17] claim that the increase of the D retention is due to Be deposition, while [8, 18] report that the C deposition increases the D retention. The C–D correlation in Be has also been investigated, on laboratory-prepared samples. Anderl *et al* found the retention in pure Be to be lower than in C-coated Be [33]. Also Guseva *et al* [34] concluded that C impurities on the Be surface enhance the D retention. On the other hand, Porosnicu *et al* irradiated different Be–C relative concentration with D ions and found that lower C concentration retained higher D content [35]. Thus, it is not clear from the literature whether the residual D retention still exists as a result of the C–D chemistry or whether D is integrated into deposits irrespective of C.

Accelerator-based ion beam analysis (IBA) is the most efficient set of methods in surface studies of wall materials [36]. Among them, a ^{3}He-based nuclear reaction analysis (NRA) has been the most frequently used for the simultaneous determination of D, Be, C in C-wall machines. In the case of JET-ILW, the C quantification on Be surfaces is not possible with the $^{12}C(^{3}He, p_0)^{14}N$ reaction due to its superposition with the $^{9}Be(^{3}He, p_3)^{11}B$ one, as detailed in [36]. The remaining options are in: (i) proton scattering via $^{12}C(p, p)^{12}C$ [37, 38] with the sensitivity at the level of 1×10^{17} ^{12}C cm^{-2}, (ii) heavy ion elastic recoil detection analysis with high sensitivity (below 1×10^{15} ^{12}C cm^{-2}) but the information depth limited to less than 1 μm, (iii) NRA using a ^{2}H beam via $^{12}C(^{2}H, p)^{13}C$. The latter method (with sensitivity of 1×10^{15} ^{12}C cm^{-2}) was applied for C studies in this paper.

A study of the C deposition on plasma-facing surfaces (PFSs) and inside the castellation grooves of JET-ILW limiters was performed earlier with a standard ^{2}H milli-beam [29]. In the current work we investigate whether C deposition on the castellation sides is affected by the orientation of the castellation side with respect to the ion or electron drift direction. Moreover, a ^{2}H micro-beam has been applied to examine the morphology of C deposition. D retention is investigated by the use of a ^{3}He micro-beam on both the PFS and the castellation sides. Whether C or D are co-deposited with Be or not cannot be verified with the present study. The overall aim is to quantify C and D on the castellation sides and PFSs of the JET-ILW Be marker tiles and investigate if C plays a role in the retention of D in the deposits.

2. Materials and experimental details

Samples from different marker tiles of the main chamber and after the first and the second experimental campaigns were investigated: one sample from the upper dump plate (DP, 2B(C)2), two from the mid-plane of outer poloidal limiter (OPL, 4D14) and four from the inner wall guard limiter (IWGL, 2XR10) (figure 1). These tiles are castellated in order to reduce the eddy currents and thermal stresses [39], and therefore, the castellation sides are free to interact with the plasma. Moreover, the samples from the marker tiles have a nickel (Ni) interlayer between the top Be layer and the bulk Be [40]. After the cut, one of the castellation sides was marked for reference reasons. The configuration of the tiles and the samples as well as the labelling of the castellation sides based on the ion/electron drift direction of ILW1 IWGL outer (27) sample, as an example, are presented schematically in figure 2.

The ^{2}H micro- and milli-beam measurements were performed using the 5.5 MV TN11 HV Tandem Accelerator at NCSR 'Demokritos', in Athens, Greece. The beam energy was 1.35 MeV and a silicon surface barrier (SSB) detector with

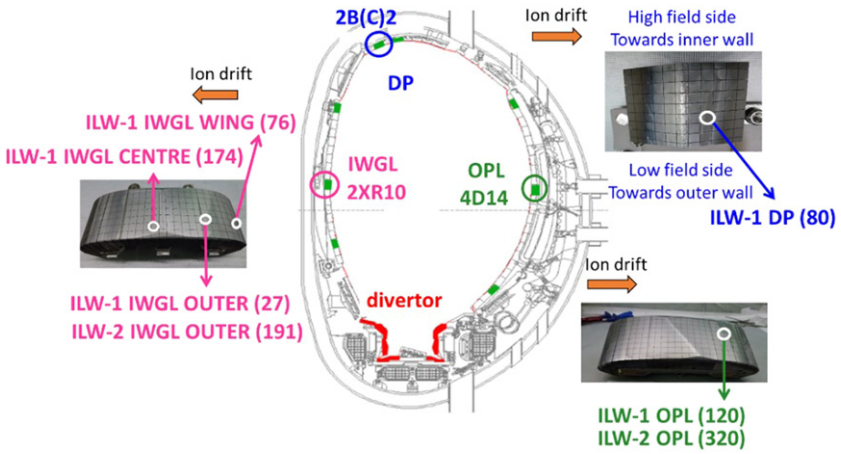

Figure 1. Position of the investigated tiles and samples inside the main chamber of the JET tokamak.

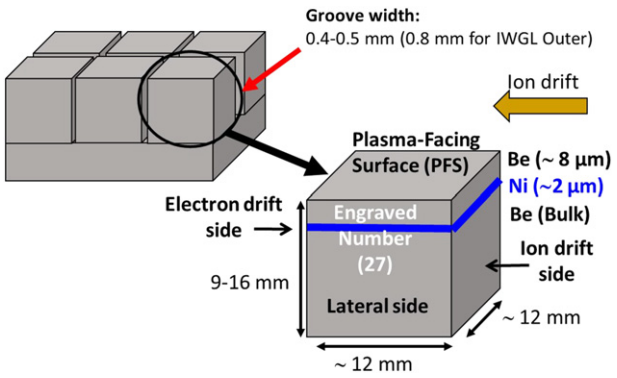

Figure 2. Schematic of the castellation configuration of the Be tiles and the configuration of the ILW1 IWGL outer (27) sample. The castellation sides are labelled based on the ion/electron drift direction.

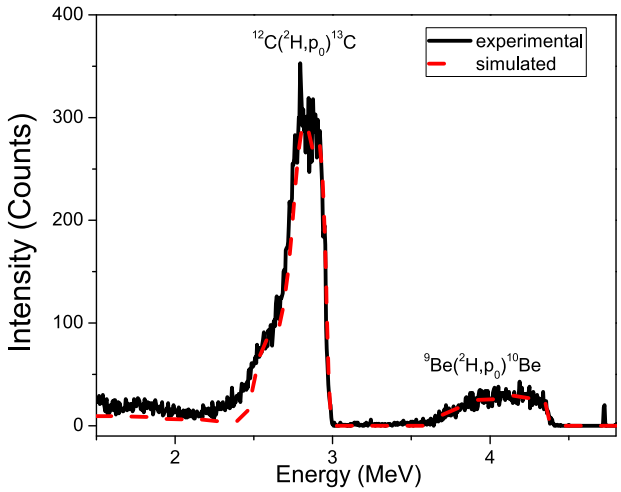

Figure 3. The measured (solid black line) and simulation (dash red line) NRA spectrum of ILW1 IWGL outer (27) castellation side using a ^{2}H micro-beam.

depletion depth of 1000 μm was placed at an angle of 170° with respect to the beam axis. A Kapton foil of 12.5 μm was positioned in front of the detector in order to separate the peak $^{12}C(d, p_0)^{13}C$ used for the C quantification from the peaks of alpha particles emitted via $^9Be(d, a_0)^7Li$ and $^9Be(d, a_1)^7Li$ reactions. The chamber was kept under vacuum (10^{-6} mbar). The beam spot of the micro-beam had a diameter smaller than 100 μm and the current was around 100 pA. The mapping area was 1.5 × 1.5 mm^2 and the resolution 64 × 64 pixels. The data acquisition and the mapping was performed using the OMDAQ2007 software and appropriate hardware [41].

The ^{3}He measurements were carried out at Ruder Boskovic Institute, in Zagreb, Croatia. The ^{3}He beam was accelerated by the 6 MV tandem Van de Graaff accelerator and 1.0 MV Tandetron accelerator. The beam energies varied between 2 and 3 MeV, and the mapping areas were either 1 × 1 mm^2 or 300 × 300 μm^2. A partially depleted SSB detector with depletion depth of 2000 μm, with nominal active area of 300 mm^2 collimated to 230 mm^2 was used and placed at an angle of 135° ± 19° with respect to the beam axis. The distance between the target and the detector was approximately 2.5 cm, which corresponds to a solid angle of 0.462 sr. Additionally, a Mylar foil of 120 μm thickness was placed before the detector in order to absorb the alpha particles produced via $^9Be(^3He, a)^8Be$ reactions and to detect only the $^9Be(^3He, p)^{11}B$ and $^2H(^3He, p_0)^3He$ peaks. A chopper was used in order to estimate the collection charge of the measurements. The data acquisition of the ^{3}He beam was performed using the in-house developed software package SPECTOR [42] and the hardware based on Xilinx Virtex 6 FPGAs; for more technical details see [43].

It is noted that the investigated area from the castellation sides is at the entrance of the gap, ranging from 0.3 to 1.5 mm into the gap, since according to Rubel *et al* [28] the majority of the D retention is restricted in this area.

The quantitative analysis of all the NRA spectra was performed with the SIMNRA software [44]. For the ^{3}He

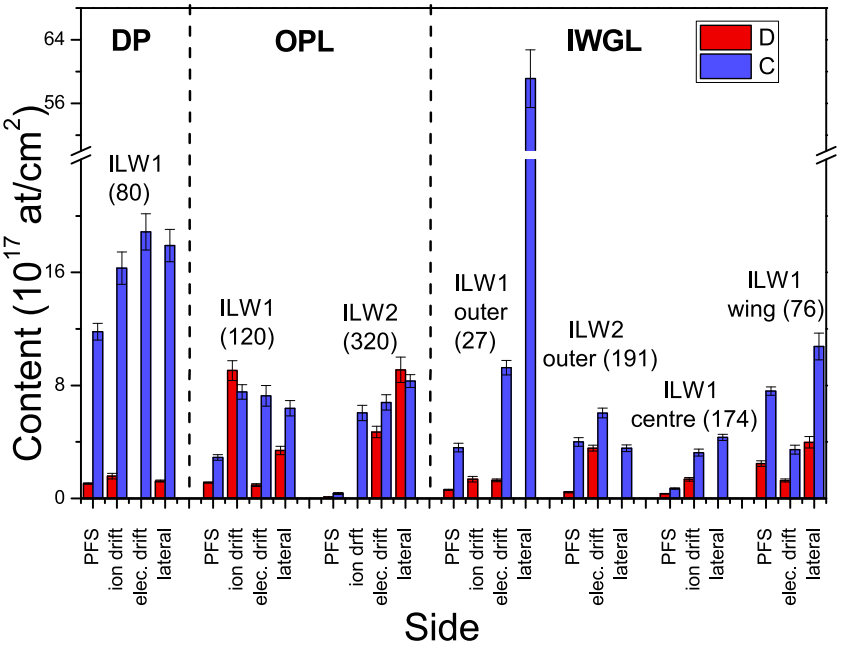

Figure 4. D and C content of the PFS and the castellation sides as measured by ^{3}He and ^{2}H beams, respectively.

micro-beam NRA measurements and the D quantification, the Alimov *et al* [45] cross section data for the ^{2}H(^{3}He, p_0)^{4}He reaction and the Barradas *et al* [46] one for the ^{9}Be(^{3}He, $p_{0,1}$)^{11}B reactions were used. For the ^{2}H beam NRA measurements and the C quantification, the evaluated cross section data from SigmaCalc archive [47] and Tsavalas *et al* [48] cross section data for the ^{12}C(^{2}H, p_0)^{13}C and ^{9}Be(^{2}H, p_0)^{10}Be reactions, respectively, were used.

3. Results and discussion

3.1. Carbon deposition

The C content was measured on ion and/or electron drift sides, as well as on some lateral castellation sides, employing a ^{2}H beam. Figure 3 presents a representative NRA spectrum together with the simulated spectrum from the lateral side of the sample 27 (ILW1 IWGL outer) using ^{2}H micro-beam. In this figure, the energy range with the peaks corresponding to the nuclear reactions ^{12}C(^{2}H, p_0)^{13}C and ^{9}Be(^{2}H, p_0)^{10}Be is shown. The quantitative results of the determined C and D amounts from (a) the PFS and (b) the castellation sides up to a maximum depth of 1.5 mm from the edge of the PFS are presented in figure 4. The absence of C or D content for some castellation sides (C content on the ion drift side of ILW1 IWGL outer (27) and D content on the ion drift side ILW2 OPL (320), the electron drift side of ILW1 DP (80), and the lateral sides of ILW1 IWGL outer (27), ILW2 IWGL outer (191) and ILW1 centre (174)) is due to the lack of experimental data. The deposited C amount on the PFS is from our previous study [29]. It is observed that the orientation of the castellation side does not, in general, affect significantly C deposition. Only for sample 27 from the ILW1 IWGL outer, almost one order of magnitude higher C amount ($(59 \pm 4) \times 10^{17}$ at/cm^2) is found for the lateral side compared to the electron drift one. On all the other castellation sides C deposition ranges from $(3.2 \pm 0.2) \times 10^{17}$ at/cm^2 to $(19 \pm 1) \times 10^{17}$ at/cm^2, with the ILW1 DP (80) presenting systematically the higher C deposition on its castellation sides and the IWGL 2XR10 centre (174) the lowest. A trend of higher C amount on the castellation sides than that on the PFS is observed.

In figure 5 the C mapping of the lateral side of all samples is depicted, with the exception of the ILW1 IWGL centre (174) sample, for which the ion drift side is presented. The PFS of the samples is at the top of the mapping and it is defined by a white line. On the ILW1 DP (80), some C agglomerates with diameter of about 150 μm have been formed over the whole side. On the ILW1 OPL (120), we observe a slight decrease of C with the depth. On the ILW2 OPL (320), C agglomerates with diameter in the range 100–200 μm are observed near the PFS of the sample. On ILW1 IWGL outer (27), at a depth of about 800 μm from the PFS, a stripe rich in C, having a width of about 500 μm, has been formed. On ILW2 IWGL outer (191), the amount of C decreases as a function of depth. On the ILW1 IWGL centre (174), 400 μm from the PFS, there is a thin stripe, having a width of about 200 μm, depleted of C. On the IWL1 IWGL wing (76), a drastic decrease of the C content with depth is observed.

3.2. Deuterium retention

The PFS and at least one castellation side of all the samples were measured using a ^{3}He micro-beam. Figure 6 depicts representative experimental and simulated spectra of the ion drift

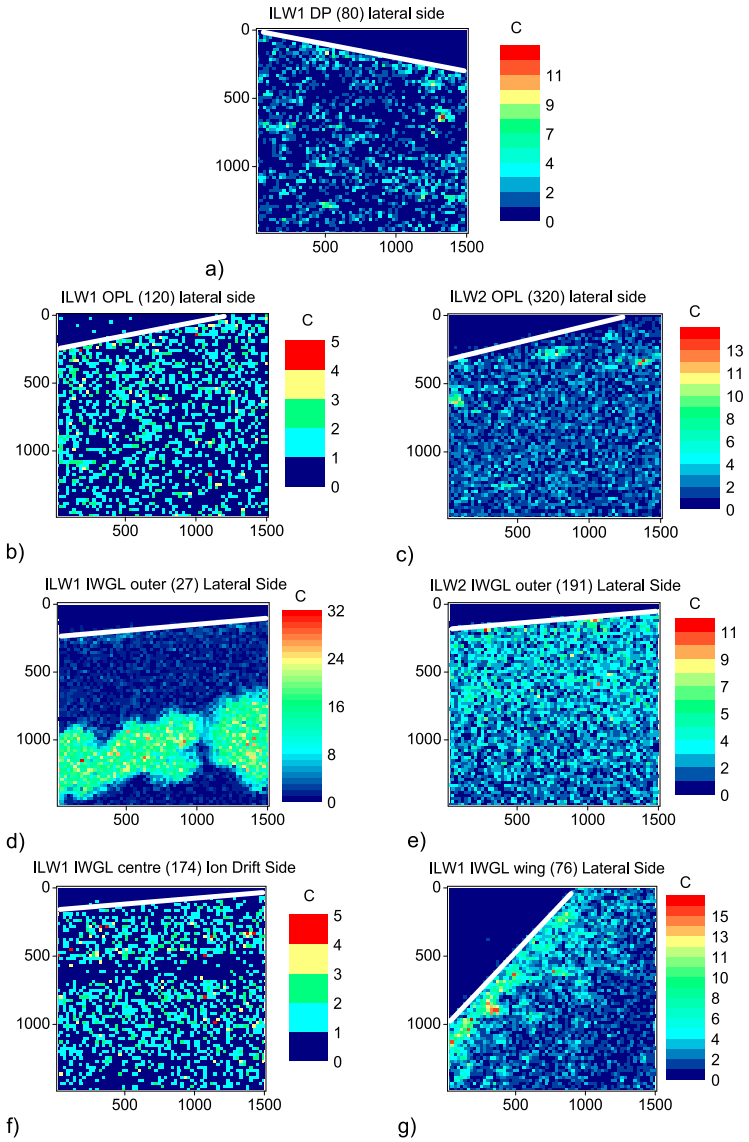

Figure 5. Mapping of the deposited C on the lateral side (*a*)–(*e*) and (*g*) and the ion drift side of the ILW1 IWGL centre (174) (*f*). The white line defines the edge of the PFS. The unit of the axes is μm.

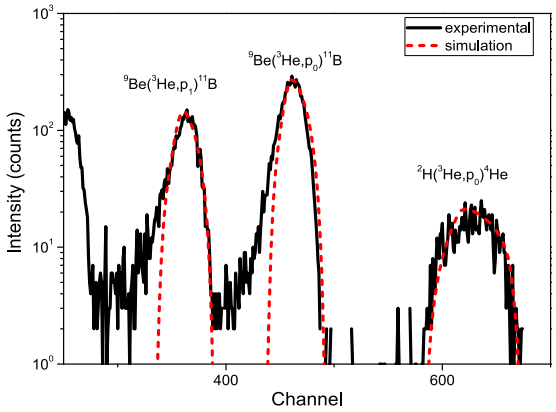

Figure 6. The experimental (black solid line) and the simulated (red dashed line) NRA spectra of the ion drift side of sample 80 from the ILW1 DP.

side from the ILW1 DP (80) employing a ^{3}He micro-beam. The determined D content using a ^{3}He beam is presented in figure 4.

The D content on the PFS of the samples is found to vary more than one order of magnitude, ranging from (0.090 $\pm$ 0.003) $\times$ 10^{17} at/cm^2 (sample 320 from ILW2 OPL) to (2.5 $\pm$ 0.2) $\times$ 10^{17} at/cm^2 (sample 76 from IWGL 2XR10 wing). The D amount determined in the current work on the PFS of ILW1 DP ((1.05 $\pm$ 0.05) $\times$ 10^{17} at/cm^2) is in reasonable agreement with that reported in [24] ((3.4 $\pm$ 1.2) $\times$ 10^{17} at/cm^2). Additionally, integrating the mean D content (1.2×10^{17} at cm^{-2}) of the different areas over the whole ILW1 IWGL tile, we observe that the total D content, 3.51×10^{19} at, is half of the corresponding value (6.76×10^{19} at) reported in [24].

On the castellation sides, the variation of the fuel retention between the various locations is reduced with the D content

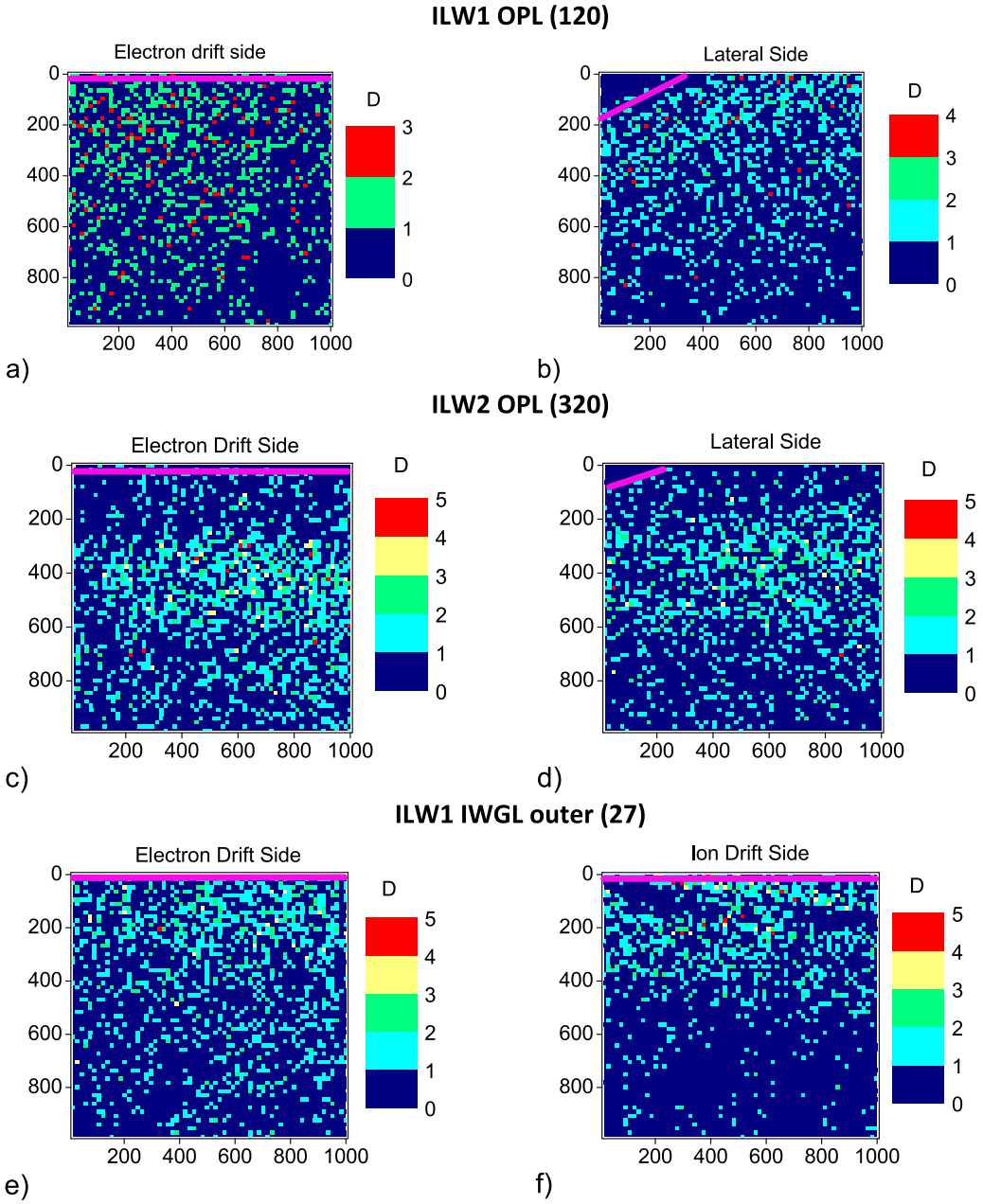

Figure 7. D mapping of castellation sides. The top magenta line defines the edge of the PFS. The unit of the axes is μm.

ranging between $(0.96 \pm 0.10) \times 10^{17}$ at/cm^2 (ILW1 OPL (120) electron drift side) and $(9.1 \pm 0.9) \times 10^{17}$ at/cm^2 (ILW1 OPL (120) ion drift side and ILW2 OPL (320) lateral side). In general the castellation sides retain higher amounts of D than the PFS.

From the first to the second campaign, the D content on the PFS decreased; for the OPL from $(1.13 \pm 0.04) \times 10^{17}$ at/cm^2 to $(0.090 \pm 0.003) \times 10^{17}$ at/cm^2 and for IWGL outer from $(0.61 \pm 0.04) \times 10^{17}$ at/cm^2 to $(0.45 \pm 0.05) \times 10^{17}$ at/cm^2. On the contrary, D amount on the castellation sides during ILW2 increases with respect to ILW1; for OPL from $(0.95 \pm 0.10) \times 10^{17}$ at/cm^2 to $(4.7 \pm 0.4) \times 10^{17}$ at/cm^2 (electron drift side) and from $(3.4 \pm 0.3) \times 10^{17}$ at/cm^2 to $(9.1 \pm 0.9) \times 10^{17}$ at/cm^2 (lateral side); and for IWGL outer from $(1.4 \pm 0.2) \times 10^{17}$ at/cm^2 to $(3.8 \pm 0.2) \times 10^{17}$ at/cm^2 (electron drift side).

Subsequently, the mean values of the D content on the castellation sides are compared with those reported in [25]. There is agreement that the ILW1 DP castellation sides present the lowest D retention with $(1.4 \pm 0.3) \times 10^{17}$ at/cm^2 found in the current work and $<10^{17}$ at/cm^2 reported in [25]. For the ILW1 OPL castellation side, the value found in the current work ($(4.5 \pm 2.4) \times 10^{17}$ at/cm^2) is very close with that reported in [25] ($\sim 6 \times 10^{17}$ at/cm^2). For the ILW1 IWGL, we find lower D amount ($(1.8 \pm 0.5) \times 10^{17}$ at/cm^2) than the low limit of the range reported in [25] ($(7–20) \times 10^{17}$ at/cm^2).

Figure 7 depicts D mappings of some of the castellation sides for IWL1 OPL (120), ILW2 OPL (320) and ILW1 IWGL outer (27), as determined with the ^{3}He micro-beam. The D distribution on the PFS is homogeneous for all samples and therefore D mappings of the PFS are not presented. On the

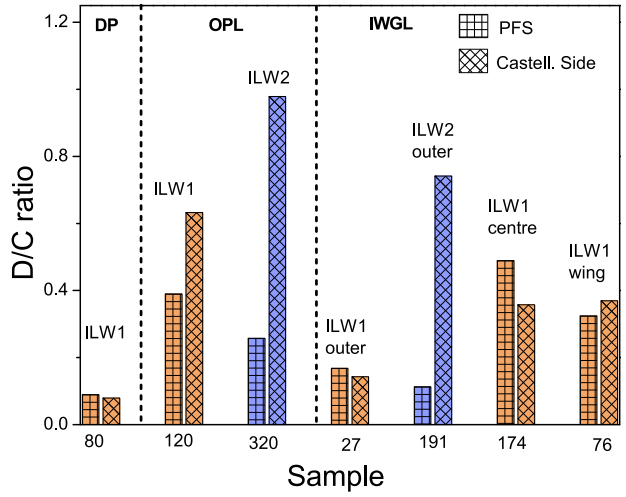

Figure 8. The D over C (D/C) ratio of the PFS and the castellation sides. For the castellation sides the average values of the measured C and D amounts have been used.

other hand, D is reduced with depth on the castellation sides of all samples apart from the ILW2 OPL (320) (figures 7(*c*) and (*d*)) where a D stripe of about 400 μm width, 200 μm from the PFS edge, is observed for both castellation sides. The D distribution is similar on the castellation sides of ILW1 OPL (120) (figures 7(*a*) and (*b*)). On the ion drift side of the IWL1 IWGL outer [27] (figure 7(*f*)) the D is reduced with depth more abruptly than on electron drift one (figure 7(*e*)).

3.3. Deuterium retention versus carbon deposition

In this section we discuss possible correlation between D retention and C deposition. From figure 4, we conclude that high C amount is not necessarily accompanied by high D content.

In figure 8 the D over C ratio (D/C) is presented for the PFS and the castellation sides. For the castellation sides the average content of C and D has been used. The D/C ratio ranges from 0.08 to 1.17 with DP presenting the smallest ratio (<0.1) and the castellation sides of OPL after the second campaign the highest one (∼1). Similar D/C ratios for the PFS and the castellation sides are observed during ILW1 campaign, whereas during ILW2 campaign the ratio is larger on the castellation sides compared to that of the PFS, being in the range of 3.8–6.6.

Next we discuss the C and D mappings from the same castellation side. Figure 9 depicts representative C and D mappings of three castellation sides. The white line defines the edge of the PFS. In figure 9(*j*) the edge of the castellation side is not well defined, because the castellation side was not perfectly aligned with respect to the ion beam so signal from the PFS was also detected.

On ILW1 DP (80) lateral side (figures 9(*a*) and (*b*)), C and D have similar homogeneous distribution all over the mapped area. On the ILW1 OPL (120) lateral side the C distribution is nearly homogeneous (figure 9(*c*)) while the D decreases with depth (figure 9(*d*)). On the ILW2 OPL (320) lateral side the stripe rich in D (figure 9(*f*)) is not observed on the C mapping (figure 9(*e*)). On the ILW1 IWGL centre (174) ion

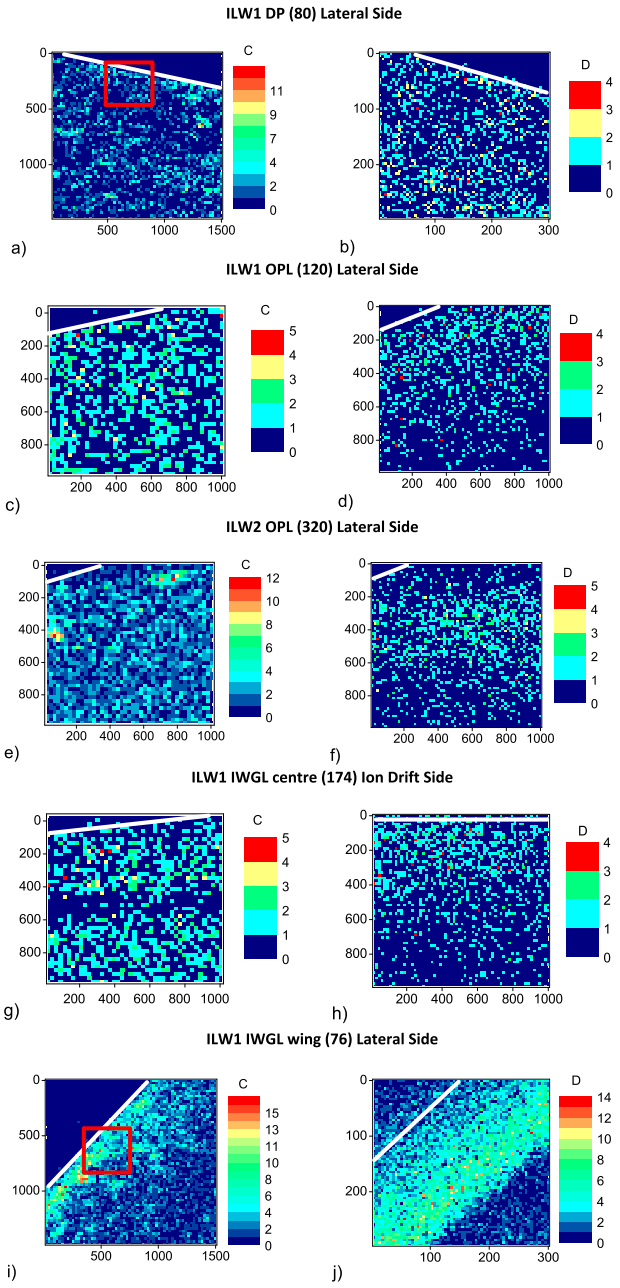

Figure 9. C and D mapping of the same castellation side of ILW1 DP (80) (*a*) and (*b*), ILW1 OPL (120) (*c*) and (*d*), ILW2 OPL (320) (*e*) and (*f*), ILW1 IWGL centre (174) (*g*) and (*h*) and ILW1 IWGL wing (76) (*i*) and (*j*). The area of D mapping for (*b*) and (*j*) corresponds to the red square of the corresponding C mapping. The white line defines the edge of the PFS. The unit of the axes is μm.

drift side, there is a zone depleted of C (figure 9(*g*)), while the amount of D decreases smoothly with depth (figure 9(*h*)). On ILW1 IWGL wing (76) lateral side, a similar stripe with high amounts of C and D is detected near the PFS (figures 9(*i*) and (*j*)).

4. Summary and conclusions

The PFS and castellation sides of samples from different Be marker tiles of the main chamber and after different campaigns

of the JET tokamak were investigated employing IBA using ^{2}H and ^{3}He beams in order to assess C deposition and D retention, respectively, their spatial distribution, their content with respect to the ion/electron drift direction and the correlation between them.

The C maps show that, in general, the C amount on the investigated castellation sides either stays constant or reduces with depth from the edge of the PFS. No systematic difference is observed in the C deposition on the different castellation sides of each sample with respect to the ion/electron drift direction.

Concerning D, the PFS of the majority of the samples has retained less of the amount than that retained on the castellation sides. From the first to the second campaign the D amount of the PFS decreases, while on the castellation sides it increases. The D distribution on the PFS is homogeneous while on the castellation sides it decreases with depth for the large majority of the samples. Additionally, the C amount is, in general, higher than the D one. No systematic correlation between the C and the D amounts has been observed.

Acknowledgments

This work has been carried out within the framework of the EUROfusion Consortium, funded by the European Union via the Euratom Research and Training Programme (Grant Agreement Nos. 633053 and 101052200—EUROfusion). Views and opinions expressed are however those of the author(s) only and do not necessarily reflect those of the European Union or the European Commission. Neither the European Union nor the European Commission can be held responsible for them. The funding from the General Secretariat for Research and Innovation of the Greek National Programme of the Controlled Thermonuclear Fusion is acknowledged. Furthermore, this project was supported by 'CALIBRA/EYIE' (MIS 5002799) which is implemented under the Action 'Reinforcement of the Research and Innovation Infrastructure', funded by the Operational Program 'Competitiveness, Entrepreneurship and Innovation' (NSRF 2014–2020) and co-financed by Greece and the European Union (European Regional Development Fund).

ORCID iDs

K. Mergia https://orcid.org/0000-0002-2633-8750
A. Widdowson https://orcid.org/0000-0002-6805-8853
M. Rubel https://orcid.org/0000-0001-9901-6296

References

[1] Barabash V., Federici G., Matera R. and Raffray A.R. (ITER Home Teams) 1999 Armour materials for the ITER plasma facing components *Phys. Scr.* **T81** 74–83
[2] Brezinsek S. *et al* (JET EFDA Contributors) 2013 Fuel retention studies with the ITER-like wall in JET *Nucl. Fusion* **53** 083023
[3] De Temmerman G. *et al* 2021 Data on erosion and hydrogen fuel retention in beryllium plasma-facing materials *Nucl. Mater. Energy* **27** 100994
[4] Coad J.P., Rubel M., Likonen J., Bekris N., Brezinsek S., Matthews G.F., Mayer M. and Widdowson A.M. (JET Contributors) 2019 Material migration and fuel retention studies during the JET carbon divertor campaigns *Fusion Eng. Des.* **138** 78
[5] Roth J. *et al* (EFDA PWI Task Force, ITER PWI Team, Fusion for Energy, ITPA SOL/DIV) 2009 Recent analysis of key plasma wall interactions issues for ITER *J. Nucl. Mater.* **390–391** 1–9
[6] Matthews G.F. *et al* 2007 Overview of the ITER-like wall project *Phys. Scr.* **T128** 137
[7] Litaudon X. *et al* 2017 Overview of the JET results in support to ITER *Nucl. Fusion* **57** 102001
[8] Coad J.P. *et al* (JET-EFDA Contributors) 2014 Surface analysis of tiles and samples exposed to the first JET campaigns with the ITER-like wall *Phys. Scr.* **T159** 014012
[9] Petersson P., Rubel M., Esser H.G., Likonen J., Koivuranta S. and Widdowson A. (JET-EFDA Contributors) 2015 Co-deposited layers in the divertor region of JET-ILW *J. Nucl. Mater.* **463** 814–7
[10] Mayer M. *et al* (JET Contributors) 2016 Erosion and deposition in the JET divertor during the first ILW campaign *Phys. Scr.* **T167** 014051
[11] Lagoyannis A. *et al* (JET Contributors) 2017 Surface composition and structure of divertor tiles following the JET tokamak operation with the ITER-like wall *Nucl. Fusion* **57** 076027
[12] Catarino N., Barradas N.P., Corregidor V., Widdowson A., Baron-Wiechec A., Coad J.P., Heinola K., Rubel M. and Alves E. (JET Contributors) 2017 Assessment of erosion, deposition and fuel retention in the JET-ILW divertor from ion beam analysis data *Nucl. Mater. Energy* **12** 559–63
[13] Zhou Y. *et al* (JET Contributors) 2017 Microanalysis of deposited layers in the inner divertor of JET with ITER-like wall *Nucl. Mater. Energy* **12** 412–7
[14] Likonen J. *et al* (JET Contributors) 2019 Investigation of deuterium trapping and release in the JET divertor during the third ILW campaign using TDS *Nucl. Mater. Energy* **19** 300–6
[15] Ström P., Petersson P., Rubel M., Fortuna-Zaleśna E., Widdowson A. and Sergienko G. (JET Contributors) 2019 Analysis of deposited layers with deuterium and impurity elements on samples from the divertor of JET with ITER-like wall *J. Nucl. Mater.* **516** 202–13
[16] Catarino N., Widdowson A., Baron-Wiechec A., Coad J.P., Heinola K., Rubel M., Barradas N.P. and Alves E. (JET Contributors) 2020 Deposition in the tungsten divertor during the 2011–2016 campaigns in JET with ITER-like wall *Phys. Scr.* **T171** 014044
[17] Krat S. *et al* (JET Contributors) 2020 Comparison of erosion and deposition in JET divertor during the first three ITER-like wall campaigns *Phys. Scr.* **T171** 014059
[18] Oya Y. *et al* (JET Contributors) 2020 Comparison of hydrogen isotope retention in divertor tiles of JET with the ITER-like wall following campaigns in 2011–2012 and 2015–2016 *Fusion Sci. Technol.* **76** 439–45
[19] Widdowson A. *et al* (JET-EFDA Contributors) 2013 Comparison of JET main chamber erosion with dust collected in the divertor *J. Nucl. Mater.* **438** S827–32
[20] Widdowson A. *et al* (JET-EFDA Contributors) 2014 Material migration patterns and overview of first surface analysis of the JET ITER-like wall *Phys. Scr.* **T159** 014010
[21] Heinola K., Ayres C.F., Baron-Wiechec A., Coad J.P., Likonen J., Matthews G.F. and Widdowson A. (JET-EFDA Contributors) 2014 Tile profiling analysis of samples from the JET ITER-like wall and carbon wall *Phys. Scr.* **T159** 014013

[22] Baron-Wiechec A. *et al* (JET-EFDA Contributors) 2015 Global erosion and deposition patterns in JET with the ITER-like wall *J. Nucl. Mater.* **463** 157–61
[23] Heinola K. *et al* (JET-EFDA Contributors) 2015 Fuel retention in JET ITER-like wall from post-mortem analysis *J. Nucl. Mater.* **463** 961–5
[24] Heinola K. *et al* (JET Contributors) 2016 Long-term fuel retention in JET ITER-like wall *Phys. Scr.* **T167** 014075
[25] Widdowson A. *et al* 2017 *Nucl. Fusion* **57** 086045
[26] Widdowson A. *et al* (JET Contributors) 2020 Fuel inventory and material migration of JET main chamber plasma facing components compared over three operational periods *Phys. Scr.* **T171** 014051
[27] Rubel M., Petersson P., Alves E., Brezinsek S., Coad J.P. , Heinola K., Mayer M. and Widdowson A. (JET Contributors) 2016 The role and application of ion beam analysis for studies of plasma-facing components in controlled fusion devices *Nucl. Instrum. Methods Phys. Res.* B **371** 4–11
[28] Rubel M. *et al* (JET Contributors) 2017 Fuel inventory and deposition in castellated structures in JET-ILW *Nucl. Fusion* **57** 066027
[29] Tsavalas P., Lagoyannis A., Mergia K., Rubel M., Triantou K., Harissopulos S., Kokkoris M. and Petersson P. (JET Contributors) 2017 Be ITER-like wall at the JET tokamak under plasma *Phys. Scr.* **T170** 014049
[30] Matthews G.F. (JET EDFA Contributors, The ASDEX-Upgrade Team) 2013 Plasma operation with an all metal first-wall: comparison of an ITER-like wall with a carbon wall in JET *J. Nucl. Mater.* **438** S2–10
[31] Loarer T. *et al* (JET-EFDA Contributors) 2013 Comparison of long term fuel retention in JET between carbon and the ITER-Like wall *J. Nucl. Mater.* **438** S108–13
[32] Brezinsek S. *et al* (JET-EFDA Contributors) 2013 Residual carbon content in the initial ITER-like wall experiments at JET *J. Nucl. Mater.* **438** S303–8
[33] Anderl R.A., Longhurst G.R., Pawelko R.J. and Oates M.A. 1997 Implanted deuterium retention and release in carbon-coated beryllium *J. Fusion Energy* **16** 95–100
[34] Guseva M.I., Gureev V.M., Danelyan L.S., Kolbasov B.N., Korshunov S.N., Sereda Y.V., Stolyarova V.G., Zatekin V.V. and Kulikauskas V.S. 2008 Effect of carbon on accumulation of deuterium in beryllium irradiated with stationary plasma *J. Surf. Investig.* **2** 274–6
[35] Porosnicu C., Anghel A., Sugiyama K., Krieger K., Roth J. and Lungu C.P. 2011 Influence of beryllium carbide formation on deuterium retention and release *J. Nucl. Mater.* **415** S713–6
[36] Mayer M. *et al* 2020 Ion beam analysis of fusion plasma-facing materials and components: facilities and research challenges *Nucl. Fusion* **60** 025001
[37] Rubel M., Coad J.P. and Pitts R.A. (Contributors to the JET-EFDA Workprogramme) 2007 Overview of co-deposition and fuel inventory in castellated divertor structures at JET *J. Nucl. Mater.* **367–370** 1432–7
[38] Rubel M., Coad J.P. and Hole D. (JET-EFDA Contributors) 2009 Overview of long-term fuel inventory and co-deposition in castellated beryllium limiters at JET *J. Nucl. Mater.* **386–388** 739–2
[39] Ricardo V., Lomas P., Matthews G.F., Nunes I., Thompson V. and Villedieu E. (JET EFDA Contributors) 2013 Design, manufacture and initial operation of the beryllium component of the JET ITER-like wall *Fusion Eng. Des.* **88** 585–9
[40] Lungu C.P., Mustata I., Zaroschi V., Lungu A.M., Anghel A., Chiru P., Rubel M., Coad P. and Matthews G.F. (JET-EFDA Contributors) 2007 Beryllium coatings on metals for marker tiles at JET: development of process and characterization of layers *Phys. Scr.* **T128** 157–61
[41] Oxford Microbeams Ltd (http://www.microbeams.co.uk/index.html)
[42] Bogovac M., Bogdanović I., Fazinić S., Jakšić M., Kukec L. and Wilhelm W. 1994 Data acquisition and scan control system for nuclear microprobe and other multiparameter experiments *Nucl. Instrum. Methods Phys. Res.* B **89** 219–22
[43] Fazinić S., Tadic T., Vuksic M., Rubel M., Petersson P., Fortuna-Zalesna E. and Widdowson A. 2018 Ion microbeam analyses of dust particles and codeposits form JET with the ITER-like wall *Anal. Chem.* **90** 5744–52
[44] Mayer M. 1999 SIMNRA, a simulation program for the analysis of NRA, RBS and ERDA *AIP Conf. Proc.* **475** 541–4
[45] Alimov V.K., Mayer M. and Roth J. 2005 Differential cross-section of the D(^{3}He, p)^{4}He nuclear reaction and depth profiling of deuterium up to large depths *Nucl. Instrum. Methods Phys. Res.* B **234** 169–75
[46] Barradas N.P., Catarino N., Mateus R., Magalhães S., Alves E., Siketić Z. and Radović I. 2015 Determination of the ^{9}Be(^{3}He, p_i)^{11}B ($i = 0, 1, 2, 3$) cross section at 135 degrees in the energy range 1–2.5 MeV *Nucl. Instrum. Methods Phys. Res.* B **346** 21–5
[47] Gurbich A.F. 2016 SigmaCalc recent development and present status of the evaluated cross-sections for IBA *Nucl. Instrum. Methods Phys. Res.* B **371** 27–32
[48] Tsavalas P., Lagoyannis A., Mergia K., Ntemou E. and Lungu C.P. 2020 Differential cross sections of the deuteron reactions on beryllium at energies and angles suitable for nuclear reaction analysis *Nucl. Instrum. Methods Phys. Res.* B **479** 205–10